



HAL
open science

Transient hillslope erosion in slow evolution landscapes

Vincent Godard, Salgado A., L Siame, Jules Fleury, Team Aster

► **To cite this version:**

Vincent Godard, Salgado A., L Siame, Jules Fleury, Team Aster. Transient hillslope erosion in slow evolution landscapes. *Earth Surface Processes and Landforms*, 2021, 46 (12), pp.2485-2500. 10.1002/esp.5190 . hal-03346897v2

HAL Id: hal-03346897

<https://amu.hal.science/hal-03346897v2>

Submitted on 16 Nov 2021

HAL is a multi-disciplinary open access archive for the deposit and dissemination of scientific research documents, whether they are published or not. The documents may come from teaching and research institutions in France or abroad, or from public or private research centers.

L'archive ouverte pluridisciplinaire **HAL**, est destinée au dépôt et à la diffusion de documents scientifiques de niveau recherche, publiés ou non, émanant des établissements d'enseignement et de recherche français ou étrangers, des laboratoires publics ou privés.

1 Transient hillslope erosion in slow evolution landscapes

2 Godard V.^{1,2,a}, Salgado A.³, Siame L.¹, Fleury J.¹ and ASTER Team^{1,*}

3 November 16, 2021

4 ¹Aix-Marseille Univ, CNRS, IRD, INRAE, Coll France, CEREGE, 13545, Aix-en-Provence,
5 France

6 ²Institut Universitaire de France (IUF), 75231, Paris, France

7 ³Department of Geography, Minas Gerais Federal University, CEP 31270-901 Belo Hori-
8 zonte MG, Brazil

9
10 ^a Corresponding author : godard@cerege.fr

11 ^{*} Georges Aumaître, Didier L. Bourlès, Karim Keddadouche

12 Published in V., Godard, A., Salgado, L., Siame, J., Fleury & ASTER Team (2021)
13 Transient hillslope erosion in slow evolution landscapes. *Earth Surface Processes and Land-*
14 *forms*, 46(12), 2485-2500 ([10.1002/esp.5190](https://doi.org/10.1002/esp.5190))

15 Abstract

16 Transient evolution and adjustment to changing tectonic and climatic boundary
17 conditions is an essential attribute of landscapes and characterizing transient behav-
18 ior is a key to understand their dynamics and history. Developing new approaches to
19 detect such transience has been explored by various methods, in particular to iden-
20 tify landscape response to Late Cenozoic and Quaternary climatic changes. Such
21 studies have often focused on regions of high relief and/or active tectonic activity
22 where interferences between tectonic and climatic signals might complicate the inter-
23 pretation of the observations. We investigated the case of the hillslopes of the Serra
24 do Cipó quartzitic range in SE Brazil in order to detect and quantify transience in a
25 tectonically-quiet landscape over 100 ka timescales. We determined hilltop cur-
26 vature from a high resolution Digital Surface Model derived from Pléiades imagery
27 and measured cosmogenic nuclide concentrations (¹⁰Be and ²⁶Al) at these hilltop

28 sites. We compare both observations with predictions of hillslope diffusion theory,
29 and observe a distinctive signature of an acceleration of denudation. We performed
30 a joint inversion of topographic and isotopic data to retrieve an evolution of hillslope
31 sediment transport coefficient through time. The timing of the increase in denuda-
32 tion cannot be unequivocally associated with a single climatic event but is consistent
33 with climatically-modulated important fluctuations in precipitation and erosion in
34 this area during Middle and Late Pleistocene.

35 **1 Introduction**

36 The Earth surface acts as a major interface between internal and external geodynamics,
37 and is the focus of many investigations concerning the complex network of processes con-
38 necting surface processes, tectonics and climate [e.g. [Champagnac et al., 2012](#)]. Notably,
39 a key element of this system is the degree of coupling between climatic variations and
40 denudation, which is fundamental to assess the strength of many postulated feedbacks
41 between the atmosphere and the dynamics of weathering, sediment production and trans-
42 port across continental surfaces. Over short time scales, many observations support the
43 key role of temperature and precipitation conditions in directly controlling the modes and
44 rates of weathering of materials transiting through regolith profiles, as well as their ex-
45 port across and beyond hillslopes domain [e.g. [Gaillardet et al., 1999](#); [Hales and Roering,](#)
46 [2005](#); [Gabet et al., 2008](#); [West et al., 2014](#)]. However, when integrating these processes
47 over larger spatial and temporal frames, highly contrasting propositions have been made
48 concerning the actual relationship between surface processes acting on continental relief
49 and climatic evolution, over the Late Cenozoic. In particular, an important question still
50 actively debated concerns whether or not Late Cenozoic cooling was associated with a
51 global increase in denudation rates [e.g. [Herman and Champagnac, 2016](#); [Willenbring and](#)
52 [Jerolmack, 2016](#); [Norton and Schlunegger, 2017](#)], suggesting that additional investigations

53 using novel methodologies are needed to better resolve denudation variations and transient
54 landscape dynamics through time.

55 Regions of high relief or tectonic activity have often been the primary target of studies
56 focusing on climate-denudation links, using the sedimentary archives resulting from the
57 erosional fluxes in such areas [e.g. [Charreau et al., 2011](#); [Lenard et al., 2020](#)]. However,
58 important limitations can be encountered in this type of settings, such as high denuda-
59 tion rates reaching the analytical limits of many measurement methods, or gaps in the
60 sedimentary records and stochastic events introducing a high degree of variability in the
61 denudation signal. Additionally, temporal and spatial variations of the tectonic boundary
62 condition can be difficult to deconvolve from the record and complicate interpretations in
63 terms of climatic influence on surface processes.

64 Conversely, areas of low tectonic activity may provide propitious conditions allowing the
65 investigation of the coupling between climate variations and surface processes. However,
66 long-duration continental sedimentary archives, spanning several 100s ka or Ma, are of-
67 ten scarce in such settings so alternative approaches are required to develop longer-term
68 records of landscape transience and assess its link with climatic evolution [[Struck et al.,](#)
69 [2018](#)]. When measuring active denudation, as opposed to paleo-denudation records in sedi-
70 mentary archives, slow landscape evolution also implies long integration timescales for most
71 geochronological techniques, such as cosmogenic nuclides, which might provide insights on
72 the dynamics of surface processes over 100s ka to several Ma. This time frame is at least
73 one order of magnitude longer to that usually encountered in active orogenic settings.

74 Terrestrial Cosmogenic Nuclides (TCN) are one of the most widely used tools to constrain
75 the distribution of denudation rates at the Earth surface over 1 ka-1 Ma timescales [[von](#)
76 [Blanckenburg, 2005](#)]. Attempts to recover information on past denudation conditions have
77 mostly focused on TCN time-series in the sedimentary record. However, combinations of
78 several cosmogenic nuclides, with different decay constants, offer the possibility to identify

79 transient dynamics resulting from changes in denudation rates through time [Mudd, 2016].
80 For example, the promising ^{10}Be - ^{14}C pair has been used to decipher complex dynamics
81 of surface processes over Holocene time scales [Hippe, 2017; Skov et al., 2019]. The more
82 common ^{26}Al - ^{10}Be system, which is classically used for burial dating studies, is much less
83 sensitive to fluctuations of denudation on this time frame [Mudd, 2016], but has been
84 shown to offer important insights over longer time scales [Knudsen and Egholm, 2018;
85 Struck et al., 2018], and its actual potential to decipher transient denudation evolution in
86 slow denudation landscapes needs to be explored more systematically.

87 Independent of chronological approaches, another way to characterize transience in land-
88 scapes, resulting from changes in denudation or incision processes, is the study of the
89 imprint of such perturbations on their morphology. Such approaches has been intensively
90 used in fluvial systems , with the analysis of river long-profiles [e.g. Roberts and White,
91 2010; Fox et al., 2015], and the increasing availability of high resolution topographic data
92 has paved the way for similar developments in the hillslope domain [Roering et al., 2007;
93 Hurst et al., 2012, 2013; Grieve et al., 2016b; Mudd, 2016]. Notably, the combination of
94 TCN data with high resolution hillslope morphological analysis has proven to be a fruit-
95 ful source of information on landscape dynamics and their response to past perturbations
96 [Godard et al., 2019].

97 In this study, we investigated the slowly eroding quartzitic landscapes of the Serra do Cipó
98 Range in Minas Gerais, Brazil, by performing both high resolution morphometric analysis
99 and cosmogenic nuclides concentration measurements (^{10}Be and ^{26}Al) at hilltop sites. The
100 observed relationships between these parameters imply an important acceleration of de-
101 nudation over 100s ka timescales and illustrate a new approach to probe into the transient
102 dynamics of landscapes as well as expanding our knowledge of Quaternary paleoclimate of
103 the central-eastern portion of South America.

2 Theoretical background

We present here the key concepts and ideas supporting our analysis of transient hillslope evolution in the Serra do Cipó. As reviewed by Mudd [2016], transient dynamics is a fundamental attribute of landscapes involving changes in their morphology, sediment fluxes or rates of denudation, and diagnostic observations can be made on these properties to identify such transient state in terms of deviation from morphological or erosional steady states. In the case of hillslopes, insights can be obtained from high resolution morphometric analysis of their shape or from denudation rates calculated from Terrestrial Cosmogenic Nuclides (TCN) concentration measurements in bedrock or stream sediments, which are two types of observations we combine in our study.

2.1 Hillslope erosion formulation

Roering et al. [1999] proposed an hillslope transport model, where sediment flux q_s is non-linearly dependant on topographic gradient dz/dx ,

$$q_s = \frac{-K(dz/dx)}{1 - [(dz/dx)/S_c]^2}, \quad (1)$$

where K is a transport efficiency, or diffusion, coefficient, z is the elevation of the topographic surface, x the horizontal coordinate and S_c a threshold gradient. Numerous field investigations have supported the validity of this formulation in high relief landscapes [e.g. Ouimet et al., 2009; DiBiase et al., 2010]. In part of the landscape where topographic gradients are small compared to the threshold S_c this relationship can simplify as,

$$q_s = -K \frac{dz}{dx}, \quad (2)$$

123 Equations 1 and 2 are Geomorphic Transport Laws [Dietrich et al., 2003], which can be
124 combined with a continuity statement,

$$\frac{dq_s}{dx} = \beta E, \quad (3)$$

125 with β the rock-to-regolith density ratio and E the long-term denudation rate, which is
126 equal to rock uplift rate when steady state is achieved. Combining equations 2 and 3 yields,

127

$$E = \frac{KC_{HT}}{\beta}, \quad (4)$$

128 where C_{HT} is hilltop curvature, the second-derivative of the topographic surface. Equation
129 4 connects together two fundamental and distinct types of observations, which can be
130 made about landscapes: measurements of their spatial topographic properties, in this case
131 C_{HT} , and measurements of their temporal rate of evolution, in this case erosion rate E .
132 For a given landscape, assessing whether these two types of observations can be reconciled
133 within the framework of equation 4 can be used as a test of the underlying steady-state
134 assumption. It should be noted that equation 4 was derived for the particular case of
135 a ridge-like hillslope system. In the following, we will rather consider isolated hills and
136 a radial symmetry for the hillslopes, which implies a slight modification of equation 4
137 [Anderson, 2002],

$$E = 2\frac{KC_{HT}}{\beta}. \quad (5)$$

138 **2.2 Detection of transience from the confrontation of morpho-** 139 **metric and TCN data**

140 Terrestrial Cosmogenic Nuclides (TCN) are now routinely used for the determination of
141 denudation rates in a variety of settings, as their steady-state concentration C in various

142 materials, such as stream sediment or outcropping bedrock, can be related to denudation
143 rate E with,

$$C = \sum_i \frac{P_i}{\frac{E\rho}{\Lambda_i} + \lambda}, \quad (6)$$

144 with P_i the TCN production rate at the surface, ρ the material density, Λ_i the cosmic ray
145 attenuation length and λ the decay constant for the considered nuclide. Subscripts i refers
146 to the various production pathways, such as spallation by neutrons or muons capture.
147 The integration time scale of these denudation rate measurements is usually calculated
148 as the time required to erode a thickness equivalent to the neutrons attenuation length-
149 scale, or ~ 60 cm in most situations [von Blanckenburg, 2005]. It results in a wide range
150 of integration windows from Ma to ka timescales for denudation rates ranging from 1 to
151 100 m/Ma, respectively. This dependency of integration time on denudation rates implies
152 that sites with different denudation rates will respond more or less rapidly, in term of
153 TCN-derived denudation rates, to perturbations of similar amplitude, and can be used to
154 identify transient adjustment in landscapes as we illustrate below.

155 If a local cosmogenic nuclides steady state is achieved at the hilltop scale, the relationship
156 between denudation rate E and hilltop curvature C_{HT} is linear and set by equation 5,
157 assuming a spatially constant value for the sediment transport coefficient K (Fig. 1).
158 Transience resulting from a change in the sediment transport coefficient through time
159 can be detected by the non-alignment of the E vs C_{HT} or $[^{10}\text{Be}]$ vs C_{HT} relationships
160 to theoretical steady-state predictions. For the case of a slow denudation landscape, we
161 assume that hillslope morphology does not change significantly over a 100 ka time-scale,
162 and do not take into account eventual feedback between denudation and hilltop curvature.

163

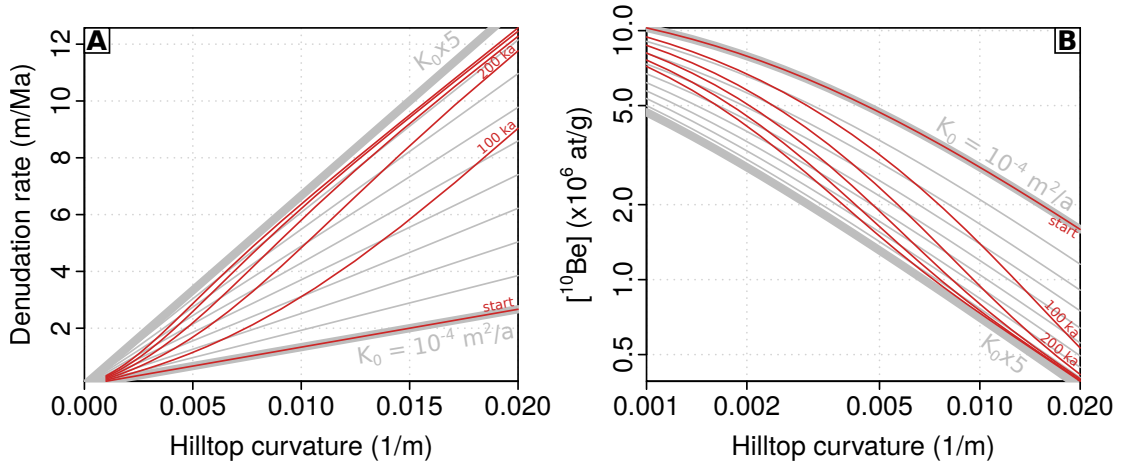


Figure 1: Illustration of the manifestation of transience in landscapes from the confrontation of cosmogenic nuclide data with high resolution topographic metrics. (A) Evolution of the relationship between hilltop curvature (C_{HT}) and ^{10}Be -derived denudation rate E , as a response to a 5-fold increase in sediment transport coefficient K . Thick grey lines are the starting and final steady-state situations. Thin grey lines are steady state relations for intermediate sediment transport coefficients (equation 5). Red curves display the transient evolution at 100 ka intervals. (B) Same as previous panel but for ^{10}Be concentration against C_{HT} (log axes). Note that we consider hillslope morphology, and thus hilltop curvature, to be stable over a time scale of a few 100s ka. This approximation is justified by the hillslope response time of the order of 1 Ma implied by the low sediment transport coefficient considered here.

164 **2.3 Detection of transience from TCN pairs**

165 As discussed by Mudd [2016], independently of morphological considerations, transience in
166 denudation can also be detected by the use of pairs of cosmogenic nuclides with different
167 decay constants. ^{10}Be - ^{26}Al is the most widely used TCN pair, notably in burial dating
168 applications [Granger and Muzikar, 2001]. However, their decay constant are of the same
169 order of magnitude, which greatly limit the sensitivity of this system for the identification
170 of transient adjustment conditions [Mudd, 2016]. Instead, this has oriented research ef-
171 forts toward the ^{10}Be - ^{14}C pair as the most promising system to resolve recent changes in
172 denudation [Hippe, 2017; Skov et al., 2019; Hippe et al., 2021]. Nevertheless, it should be
173 noted that in the particular case of slowly eroding landscapes, where the ^{10}Be and ^{26}Al
174 half-lives are comparable with the TCN denudation integration timescale, the amplitude of
175 the deviation of isotopic ratio away from steady-state denudation predictions can become
176 analytically resolvable (Fig. 2). This deviation is particularly noticeable for an increase
177 in denudation rate, as it significantly lowers the ratio below the steady-state denudation
178 curve. The time-scale of the perturbation being also dependent on the denudation rate, the
179 transient response can thus be observed over a few 100s ka in the case of slowly evolving
180 landscapes (1 m/Ma).

181 **3 Settings**

182 Our study area is located in the Serra do Cipó national park, in the highlands of the
183 Brazilian Southeast. The Serra do Cipó mountain is a narrow (30-km wide) quartzitic
184 range located in the southern portion of the Espinhaço Range (Fig. 3), which is the most
185 extensive and continuous Precambrian orogenic belt of the South American Platform and
186 originated 600 Ma ago during the Brazilian Orogeny [Magalhães Junior et al., 2015]. The
187 Espinhaço Range is an important hydrographic and landscape divider in South America.

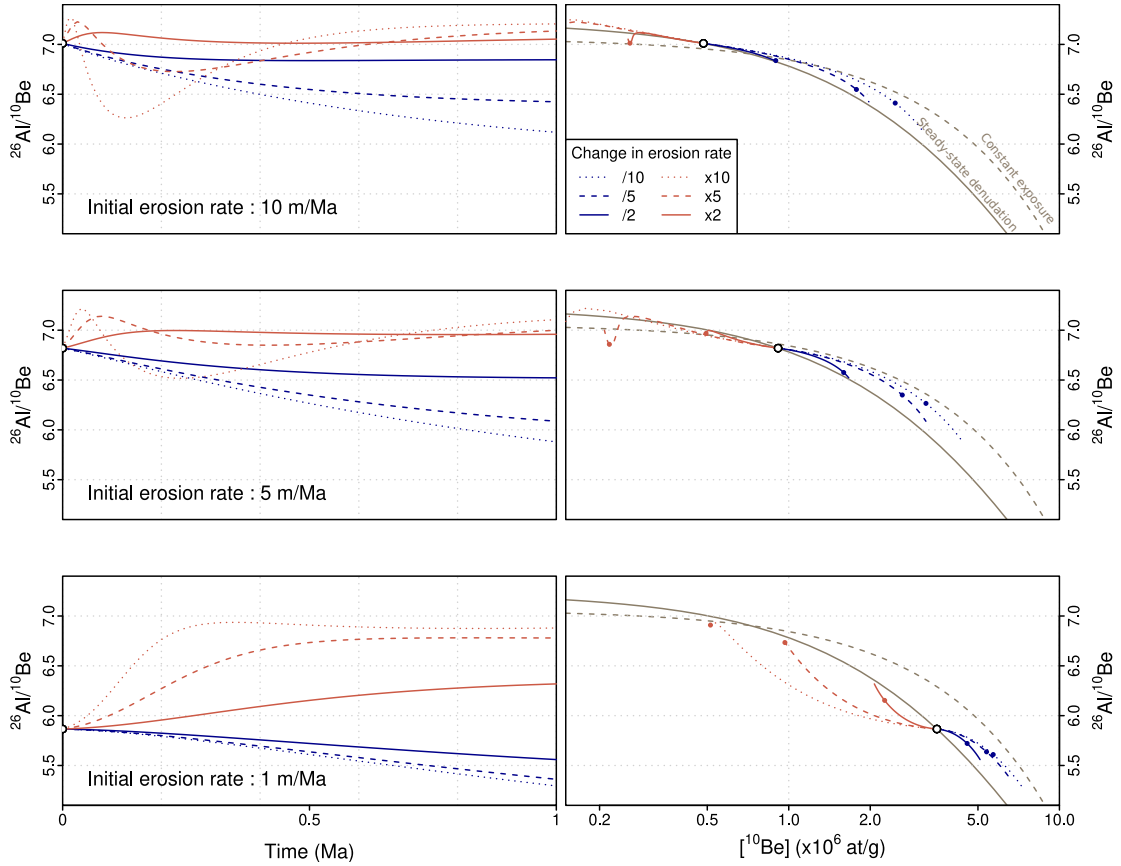


Figure 2: Responses of ^{10}Be and ^{26}Al surface concentrations and ratio to 2, 5 and 10-fold increases or decreases in denudation rates. Left panels display the evolution through time of the $^{26}\text{Al}/^{10}\text{Be}$ ratio, since the onset of the perturbation. Right panels display the corresponding evolution in a two-nuclides plot. White and colored circles indicate the starting points and 0.5 Ma mark, respectively. Solid and dashed brown curves correspond to expectations for steady-state erosion and a constantly exposed surfaces, respectively. Production rates are calculated for the average conditions at the sampled sites in the Serra do Cipó (Fig. 3), using a time-independent scaling scheme [Stone, 2000].

188 To the west is located the large hydrographic basin of the São Francisco River, which drains
189 a craton characterized by smooth relief, semi-humid climate, and savanna vegetation. To
190 the east, drainage is organized around smaller watersheds, such as the Doce and Jequit-
191 inhona hydrographic basins, that drain a half-orange hills plateau-type landscape, under
192 humid climate and tropical forests [Salgado et al., 2019].

193 After its uplift during the Brazilian Orogeny, the Serra do Cipó has not been subjected to
194 new orogenic phases and the subsequent erosion of the range resulted in a relief character-
195 ized by a wide quartzitic plateau (average elevation 1200 m), comprising a large sequence
196 of ridges, reaching 2000 m in altitude, depressions and dissected fluvial valleys. There are
197 no evidence of a direct impact of the opening of the South Atlantic on our study area.
198 Although landscape properties are globally homogeneous across the Serra do Cipó, the
199 portion of the range that drains towards the Doce River is more dissected than that drain-
200 ing into the São Francisco River.

201 Nowadays, the climate of Serra do Cipó Range is mesothermal, with Mean Annual Temper-
202 ature between 18°C-19°C and Mean Annual Precipitation ranging from 1250 to 1550 mm,
203 as well as dry winters and wet summers. However, there are lines of evidence, from pedo-
204 logical and geomorphological records, that the region underwent many climatic changes
205 during the Holocene and late Pleistocene, with occurrences of periods wetter and dryer
206 than the present-day conditions [Chueng et al., 2019; Barros and Magalhães Junior, 2020;
207 Silva et al., 2020].

208 Due to the great resistance of the quartzite bedrock to erosion, denudation rates are <6
209 m/Ma [Barreto et al., 2013; Peifer et al., 2020], soils are thin and poor, hosting the typi-
210 cal vegetation of Campos Rupestres, a high altitude rocky field biome [Magalhães Junior
211 et al., 2015]. This combination of slow denudation rates and significant relief is well suited
212 for the coupling of high-resolution morphometry and cosmogenic nuclides analyses due to
213 long-integration time scales for denudation, a limited contribution of stochastic events to

214 surface processes, a limited storage of erosion products and long relief response timescales.

215

216 4 Methods

217 4.1 General sampling strategy

218 Our strategy was to select prominent sites on top of soil-mantled vegetation-free hillslopes
219 (Fig. 4), where the observed denudation rates E and morphological properties such as
220 hilltop curvature C_{HT} could be linked into the simple physical framework of equation 5
221 [Anderson, 2002; Hurst et al., 2012]. The slope of this relationship between E and C_{HT} is
222 set by the sediment transport coefficient K and the rock-to-regolith ratio β .

223 We primarily selected regolith-mantled hilltop sites, with regular morphologies and no
224 bedrock outcrops (Fig. 4A-B). We sampled quartz fragments resulting from the disman-
225 tlement of quartz veins embedded in the fine-grained quartzite bedrock and sandy regolith
226 (Fig. 4C). At some sites, the quartz veins were directly outcropping, but not significantly
227 protruding over the surface, and the quartz fragments were detached directly from the
228 veins (Fig. 4D). At other sites, the veins were not directly outcropping, but covered by
229 10 to 20 cm of regolith. We observed that the quartz veins remain coherent and resistant
230 during their exhumation toward the surface, whereas the fine grained quartzite bedrock
231 is converted into sandy regolith. Site O is an exception, where we directly sampled the
232 outcropping quartzite bedrock.

233 4.2 Cosmogenic nuclides analysis

234 Samples for ^{10}Be and ^{26}Al concentrations measurements were collected at 11 hilltop sites,
235 by amalgamating 30 to 40 individual quartz vein fragments at the surface (except for site

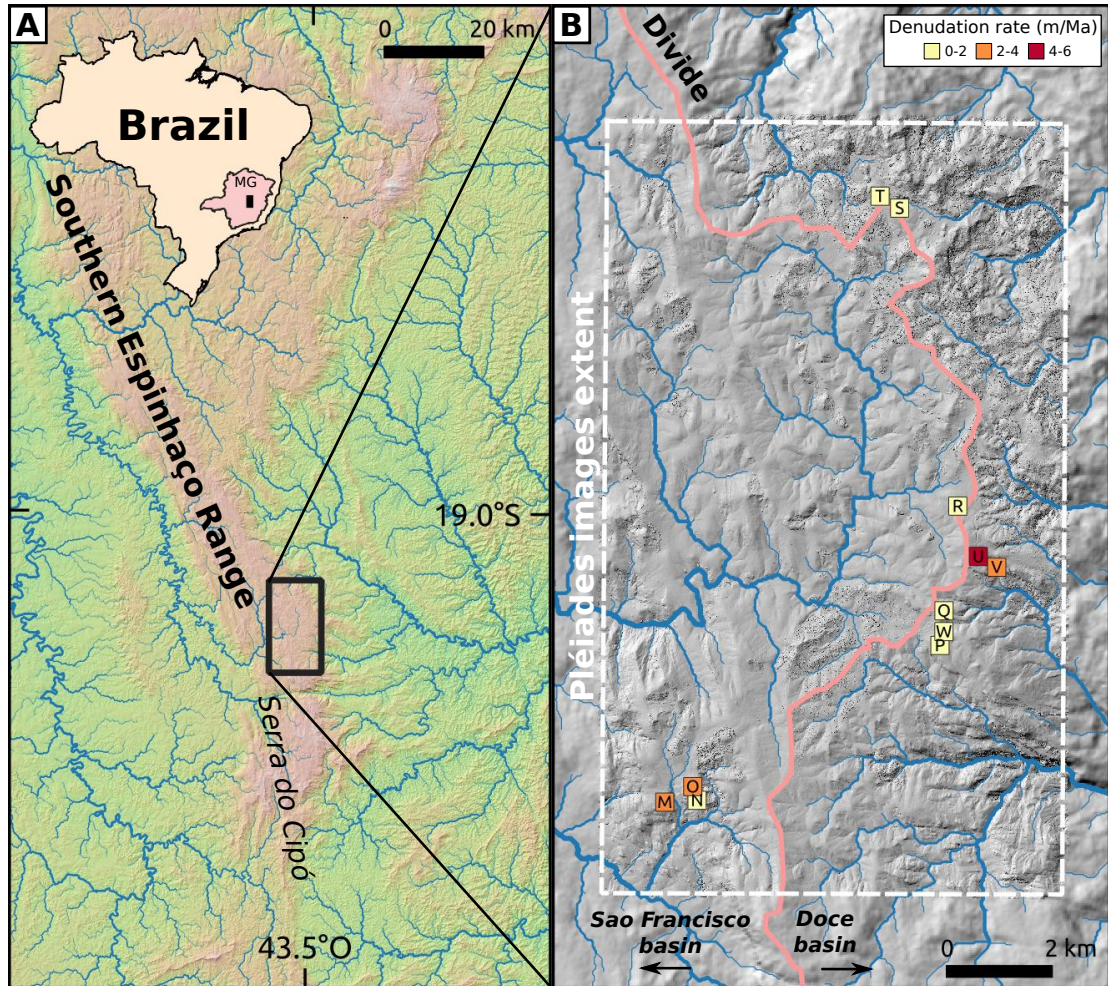


Figure 3: (A) Situation of the Southern Espinhaço Range in Minas Gerais State. (B) Location of sampled hilltop sites in the Serra do Cipó Range. Color scale indicates calculated steady-state denudation rates from ^{10}Be concentrations (m/Ma). Dashed rectangle is the extent of the Pléiades images triplet used to compute a high resolution Digital Surface Model (DSM). Pink line is the divide between the São Francisco and Doce river basins.

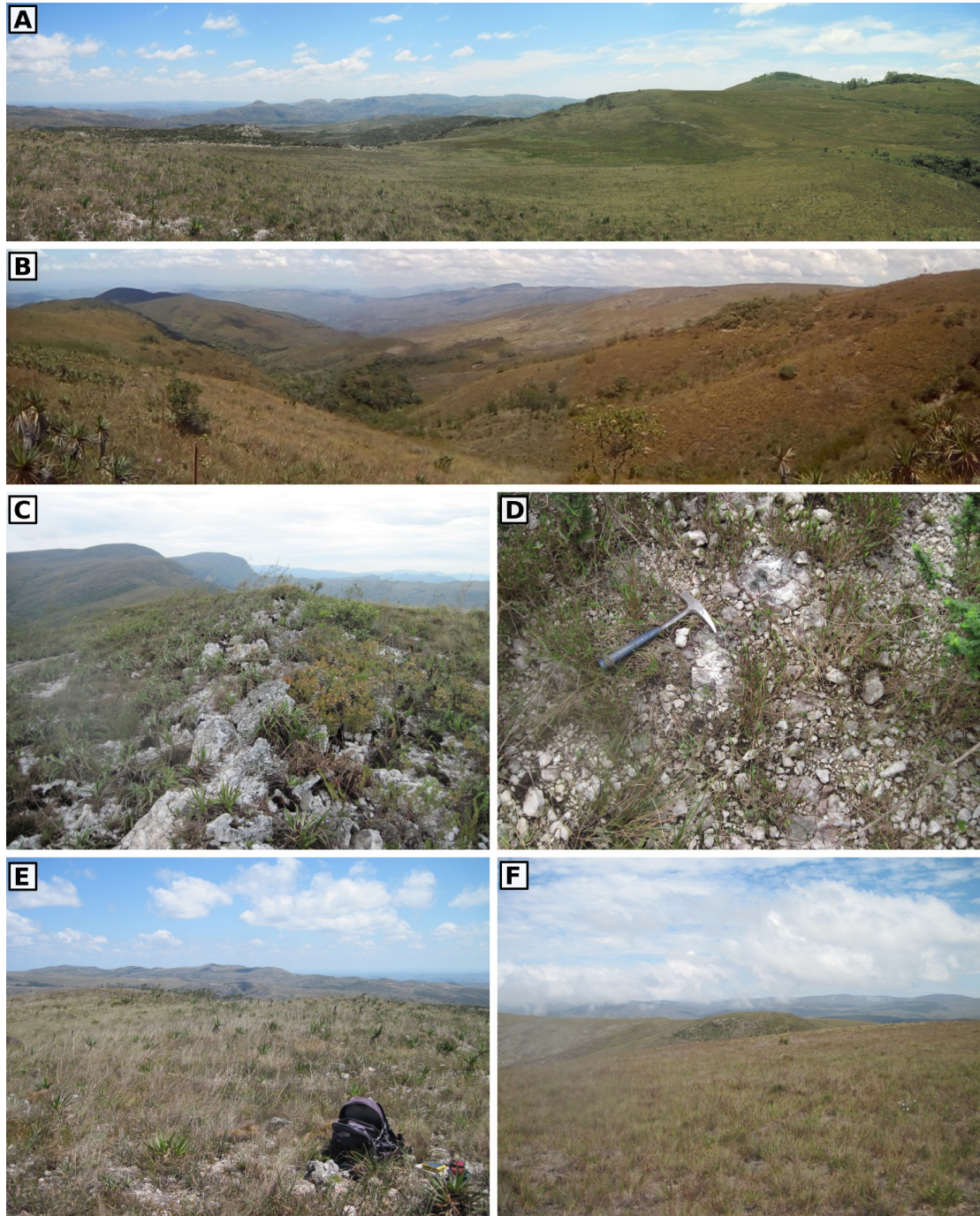


Figure 4: Sampling sites pictures. (A) View on Serra do Cipó landscape, toward the East from site M. (B) View on Serra do Cipó landscape, toward the East from site T. (C) Quartz vein at hilltop sampling site N. (D) Surface of hilltop sampling site W, with quartz vein embedded in the regolith and small quartz fragments. (E) Hilltop sampling site M. (F) View toward site W.

236 O). Samples were crushed and sieved to extract the 250-1000 μm fraction, which was sub-
237 mitted to sequential magnetic separations. The remaining fraction was leached with 37%
238 HCl to remove eventual carbonate fragments. The samples were then repetitively leached
239 with H_2SiF_6 and submitted to vigorous mechanical shaking until pure quartz was obtained.
240 Decontamination from atmospheric ^{10}Be was achieved by a series of three successive leach-
241 ings in concentrated HF, each removing 10% of the remaining sample mass [Brown et al.,
242 1991]. After addition of Be and Al carriers, the samples were digested in concentrated HF.
243 Be and Al were isolated for measurements using ion-exchange chromatography. $^{10}\text{Be}/^9\text{Be}$
244 and $^{26}\text{Al}/^{27}\text{Al}$ measurements were performed at the French AMS National Facility, located
245 at CEREGE in Aix-en-Provence. All results and technical characteristics of the measure-
246 ments and calculations are provided in tables 1 and 2.

247 For reference, and before investigating time-variations in denudation, we compute steady-
248 state denudation rates (tables 1 and 2), which were calculated with the online calculator
249 described in Balco et al. [2008] and the nuclide specific LSD scaling scheme of Lifton et al.
250 [2014], using the CRONUS-Earth calibration dataset [Borchers et al., 2016] for the calcu-
251 lation of spallation production rates and muon production rates according to Balco [2017].
252 We used 160 g/cm^2 for the effective neutron attenuation length in rock, and a density of
253 2.65 g/cm^3 . No shielding correction was considered for the hilltop sites we sampled.

254 4.3 Morphometric analysis

255 We acquired a triplet of Pléiades images covering our sampling area (Fig. 3B), and used
256 photogrammetric techniques to construct a 1 m resolution Digital Surface Model (DSM) and
257 perform hilltop curvature calculations. Pléiades satellites provide panchromatic images
258 with a 0.7 m resolution resampled at 0.5 m pixel size, and have the capacity to acquire
259 multi-stereo views of a scene during the same orbit [Bernard et al., 2012]. In low vegeta-
260 tion settings, they provide an efficient and cost-effective alternative to airborne LiDAR to

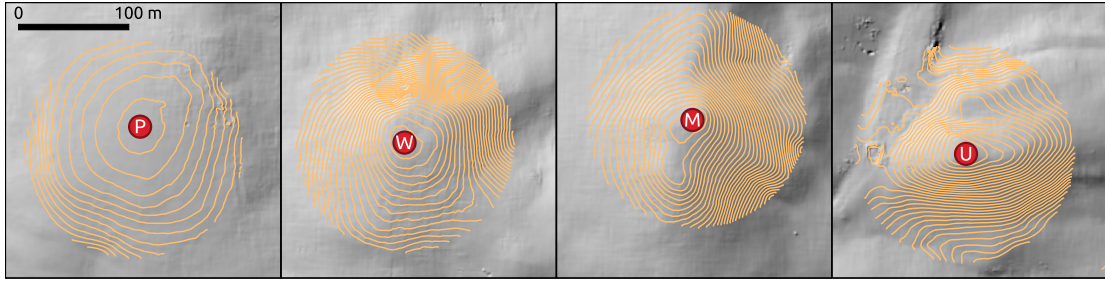


Figure 5: Shaded Pléiades Digital Surface Model (DSM) for 4 selected hilltop sites. Spacing of elevation contours is 1 m.

261 produce high-resolution Digital Elevation Models over large areas [e.g. [Ansberque et al.,](#)
 262 [2016](#)]. While this type of imagery, and derived topographic data, has been extensively used
 263 in tectonic geomorphology investigations since the launch of the satellites in 2011, its use
 264 in quantitative process-oriented geomorphological studies is less common [[Godard et al.,](#)
 265 [2019](#)]. A triplet of Pléiades images was acquired by instrument PHR1A on the 5th of July
 266 2019 over a $\sim 250 \text{ km}^2$ area, covering the hilltop sites studied here.

267 The image triplet was processed with NASA AMES Stereo pipeline [[Broxton and Edwards,](#)
 268 [2008](#); [Moratto et al., 2010](#)] in order to produce a Digital Surface Model (DSM). We used the
 269 Rational Polynom Coefficients (RPC) provided with the images for the internal calibration
 270 of the pushbroom sensor. No Ground Control Points were used during the processing. The
 271 images were first roughly aligned by orthorectification on WGS84 datum using a SRTM
 272 Digital Elevation Model. Low-resolution disparity maps for couples of images were com-
 273 puted to determine coarse correspondence between pixels. Sub-pixel refinement was then
 274 performed using an adaptive window correlator [[Nefian et al., 2009](#)]. The disparity map
 275 was filtered by removing pixels with a value differing from the mean of their neighborhood
 276 by more than 3. The point cloud was triangulated and gridded to produce a 1-m resolution
 277 Digital Surface Model (Figs. [3](#) and [5](#)).

278 In order to compute hilltop curvature C_{HT} , we fitted a quadratic surface to the DSM
 279 elevation over a circular window centered on the sampling point [[Hurst et al., 2012](#)]. The

280 equation of the surface is,

$$z = ax^2 + by^2 + cxy + dx + ey + f. \quad (7)$$

281 Topographic curvature C_{HT} is computed as the two-dimensional Laplacian of the quadratic
282 surface as,

$$C_{HT} = 2a + 2b \quad (8)$$

283 The radius of the analysis window was chosen to be large enough to filter short-wavelength
284 surface roughness, and small enough to avoid perturbation from the ridge-and-valley to-
285 pographic signal [Lashermes et al., 2007; Roering et al., 2010; Hurst et al., 2012; Godard
286 et al., 2016; Grieve et al., 2016a]. In our case, this radius was set at 10 m (Fig. 6). In
287 order to account for uncertainties on the position of the sampling sites and the influence
288 of small wavelength topographic fluctuations, we computed C_{HT} at each pixel within a 10
289 m radius of the sampling point, and then calculated the mean and standard deviation of
290 these values.

291 4.4 Numerical modeling

292 We predicted the concentrations in ^{10}Be and ^{26}Al at the surface by considering the pro-
293 gressive accumulation of these cosmogenic nuclides during exhumation as a response to
294 imposed time-varying denudation, using a Lagrangian point of view [Knudsen et al., 2019].
295 We used the CRONUS-Earth calibration dataset [Borchers et al., 2016] and nuclides specific
296 time-dependent LSD scaling scheme [Lifton et al., 2014], for the calculation of spallation
297 production rates. Muons production was computed following Model 1A and associated
298 parameters from Balco [2017]. We used 160 g/cm² for the effective neutron attenuation
299 length in rock, and a density of 2.65 g/cm³.

300 The originality of our approach is that the denudation rate E at our sites of interest is

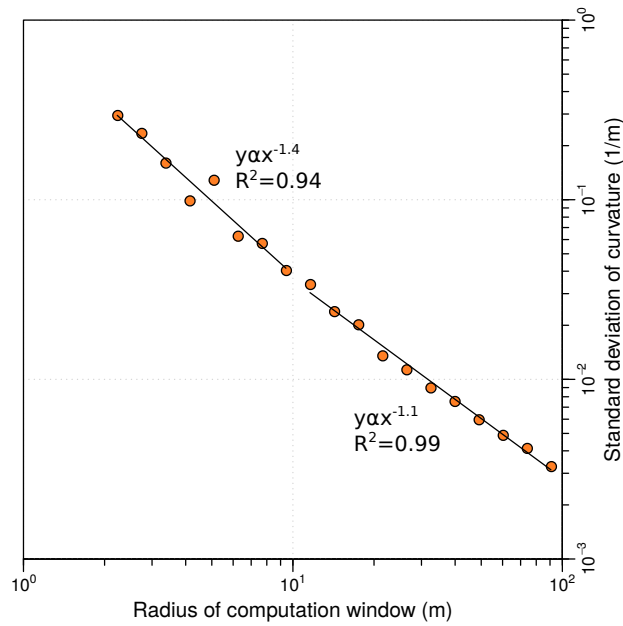


Figure 6: Evolution of the standard deviation of curvature as a function of the radius of the analysis window used to fit the quadratic surface of equation 7. 80×10^3 measurement points were sampled from the Pléiades DSM. A slight scaling break occurs at ~ 10 m radius for the analysis window and this size is used in the curvature computation. We note that the scaling break is less pronounced than in the results of Roering et al. [2010], due to the gentler variations in elevation of the Serra do Cipó hillslopes and the absence of trees, as opposed to the rugged and densely forested landscape of the Oregon Coast Range.

301 computed from their measured hilltop curvature C_{HT} according to equation 5. This al-
 302 lows us to impose time-variations in denudation through changes in K , affecting all sites
 303 synchronously, rather than considering the evolution of denudation rates at each site indi-
 304 vidually. In other words, this allowed us to perform a joint inversion of a single K history
 305 to assess the changes in denudation through time, rather than dealing with the 11 inde-
 306 pendent denudation histories at each site separately.

307 We parameterized the evolution of the sediment transport coefficient K through time as a
 308 two-steps history, which is thus defined by three parameters : (1) the sediment transport
 309 coefficient K_1 during an initial slow denudation phase, (2) the sediment transport coeffi-
 310 cient K_2 during a recent faster denudation phase and (3) the transition time T between the
 311 two phases. Similar scenarios of hillslope evolution based on a two-steps history for the sed-
 312 iment transport coefficient were explored by [Roering et al. \[2004\]](#) over shorter timescales,
 313 and allowed to capture the impact of a climate changing event while limiting the number of
 314 free parameters. A significant amount of scatter is expected in our dataset, which is usual
 315 in the type of complex natural system we are dealing with. Our forward model is based
 316 on a simplified definition of the problem, which does not account for numerous processes
 317 complicating hillslope dynamics and are not captured by idealized relationships such as
 318 equation 5. Additionally, the two-steps scenario we used is a coarse, but necessary, simpli-
 319 fication of the actual denudation history. Such epistemic uncertainty is not represented by
 320 the measurement errors on either the ^{10}Be concentrations or hilltop curvatures. For that
 321 reason, we do not expect the modelled concentrations C_{mod} to be able to fit the observed
 322 concentrations C_{obs} within these measurement errors. We introduce a residual error σ_e as
 323 a 4th parameter which is sampled along the ones described above [[Laloy et al., 2017](#)], with
 324 a likelihood defined as,

$$L(K_1, K_2, T) = \frac{1}{\sqrt{2\pi}\sigma_e} \exp\left(\frac{-1}{2\sigma_e^2} \sum_{i=1}^n (C_{obs,i} - C_{mod,i}(K_1, K_2, T))^2\right), \quad (9)$$

325 where n is the total number of observed TCN concentrations used in the inversion. We used
326 a standard Monte Carlo-Markov Chain (MCMC) approach to move through the parameter
327 space and estimate the posterior distributions [Metropolis et al., 1953].

328 5 Data

329 At hilltops, the measured ^{10}Be concentrations range from 0.8 ± 0.02 to 6.9 ± 0.1 10^6 at/g
330 (Fig. 7A and table 1), which corresponds to steady denudation rates of 6 ± 0.5 to 0.35 ± 0.05
331 m/Ma, respectively. The $^{26}\text{Al}/^{10}\text{Be}$ ratios range from 4.4 ± 0.1 to 6.4 ± 0.2 , with 6 samples
332 plotting within the erosion island, slightly above the steady state erosion curve (Fig. 7A
333 and table 2). These samples are evenly distributed over the range of observed ^{10}Be con-
334 centrations. One sample (R) presents an anomalously high ratio, which is impossible to
335 obtain by TCN accumulation and decay. It is probably affected by an analytical issue on
336 the determination of the ^{27}Al concentration, which is significantly higher than the rest of
337 the dataset (except sample O). Only the ^{10}Be concentration will be used for this sample
338 in the following. Finally, 4 samples display ratios clearly below steady-state denudation
339 predictions, including the 3 samples with the lowest ^{10}Be concentrations.

340 At our sampling sites, measured hilltop curvatures span an order of magnitude from 0.005
341 to 0.039 m^{-1} (Fig. 7B and table 3). Denudation rates, calculated under a steady state
342 assumption, increase with hilltop curvature. We note that sample O is slightly off the gen-
343 eral trend and corresponds to the only site where we sampled the outcropping quartzite
344 bedrock, instead of the quartz veins.

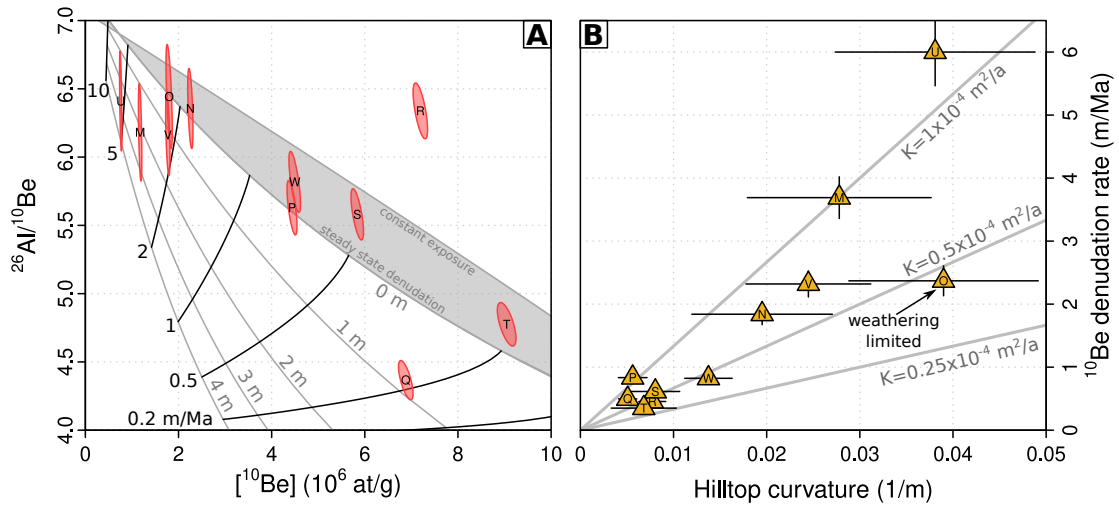


Figure 7: (A) Two-nuclides plot for the samples collected at hilltops (1σ confidence ellipses). See figure 3 for sites locations. Grey-filled area indicates the region between the steady-state surface denudation and constant exposure scenarios. Grey and black lines correspond to various regolith mixing-depth and denudation rates, respectively, according to the model of Foster et al. [2015]. Scaling according to Stone [2000]. (B) Denudation rate calculated from measured ^{10}Be concentrations as a function of hilltop curvature computed from the Pléiades DSM. Grey lines correspond to equation 5 with various values of the sediment transport coefficient.

6 Discussion

6.1 Interpretation of observed TCN concentrations

The denudation rates calculated under a steady-state assumption span a large range, from 0.5 to 6 m/Ma. Barreto et al. [2013] reported denudation rates of 1.8 to 2.4 m/Ma and 4.0 to 6.3 m/Ma for catchments located in the São Francisco and Doce river basins, respectively.

The global range of denudation rates reported for these catchment wide denudation rates is largely overlapping with our local measurements near the drainage divide. We do not observe systematic gradient in denudation rates at our sites between the two sides of the divide, as in the results of [Barreto et al., 2013], and the diversity of denudation rates in our dataset probably reflects an underlying long-standing diversity in hillslope and hilltop morphologies across the relict landscape of the Serra do Cipó uplands.

Some of our samples present $^{26}\text{Al}/^{10}\text{Be}$ ratios that are significantly lower than steady-state denudation predictions (sites Q, M, U and V). Such low ratios are usually interpreted as reflecting temporary burial of the material [Granger and Muzikar, 2001] where, in the absence of TCN production, the differential rate of decay between the two isotopes is progressively lowering the ratio. However, such explanation is highly unlikely for our samples collected at the top of continuously eroding prominent hilltop sites, where there is no evidence for any significant potential for long-term storage and burial. Regolith mixing in slowly eroding soil profiles can also induce a lowering of $^{26}\text{Al}/^{10}\text{Be}$ ratios below the steady-state denudation line [e.g. Makhubela et al., 2019]. While this process could explain the measured ratio at site Q, it is difficult to reconcile with field observations at the other sites where we directly sampled outcropping veins. Furthermore, these three sites (M, U and V) display the highest denudation rates, and are eroding almost an order of magnitude faster than the slowest sites of the dataset. The last possible process to explain the observed low $^{26}\text{Al}/^{10}\text{Be}$ ratios at sites M, U and V is an increase of denudation rate [Struck et al.,

370 2018], which would dominantly impact the fastest sites with short integration time scales
371 (100-200 ka, table 1) and much less the slowest sites, which average denudation over a longer
372 time-frame (Fig. 2). Independent of any consideration on the morphology of the studied
373 sites, our TCN data present evidence of transience and acceleration of denudation rates in
374 the past. The amplitude and timing of such increase is however difficult to constrain from
375 ^{26}Al - ^{10}Be data alone.

376 6.2 Relationship between TCN data and hilltop morphology

377 The relationship between denudation rate E and hilltop curvature C_{HT} (equation 5) is
378 not linear (Fig. 7B), as would be expected from hillslope diffusion theory [Anderson, 2002;
379 Hurst et al., 2012]. No single sediment transport coefficient can explain the data within un-
380 certainty, and we observe a systematic tendency for the sites with higher denudation rates
381 (lower integration time scale) to plot on a higher K line, when compared to the slower
382 ones. In line with our previous observations on the $^{26}\text{Al}/^{10}\text{Be}$ ratios, this constitutes an
383 additional evidence for an acceleration of denudation over our area of interest (Fig. 1). We
384 note that a recent large-scale compilation by Gabet et al. [2021] have also identified non-
385 linearity in the relationship between C_{HT} and TCN-derived denudation rates but further
386 investigations are needed to assess its signification in terms of hillslope dynamics.

387 In order to obtain more quantitative insights on this postulated acceleration of denuda-
388 tion, we tested a 2-stage denudation history defined by 3 parameters : the transition time
389 between the slow and fast periods of denudation and their respective sediment transport
390 coefficients (Fig. 8). We predicted ^{10}Be concentrations at the sites of interest for any
391 combinations of these parameters, using the measured hilltop curvature (C_{HT}) to compute
392 denudation rates evolution through time using equation 5, and perform a MCMC driven
393 inversion. The sampling of the parameter space is driven by the Metropolis-Hasting algo-
394 rithm, with an acceptance rate of 32%. We ran 16 independent chains, each 5×10^5 , in

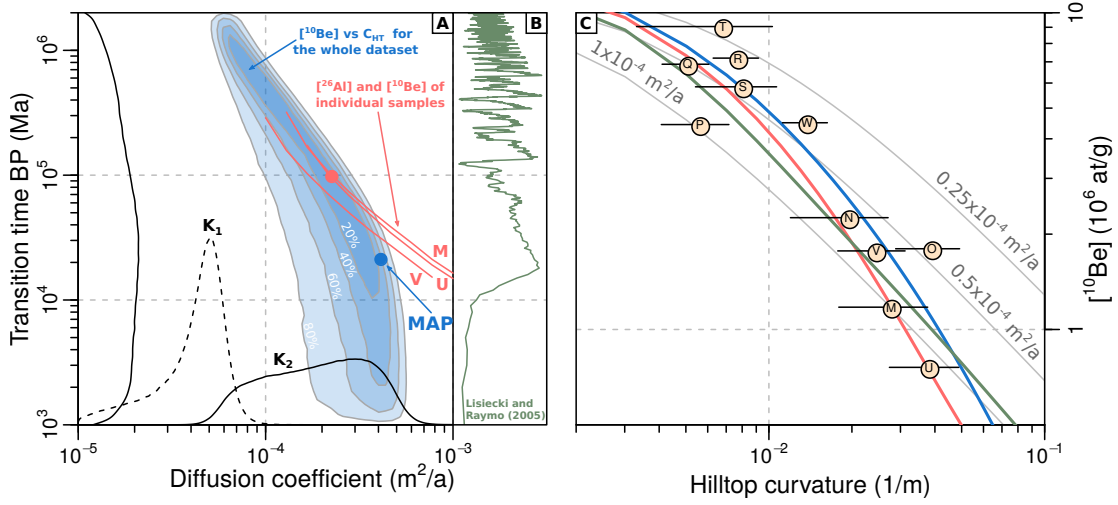


Figure 8: (A) Result of the MCMC inversion based on a 2-stages history set by 3 parameters: the initial (K_1) and final (K_2) sediment transport coefficients and the transition time T between the two. Blue shaded contours are highest posterior density region for T against K_2 , and the filled blue circle indicates the Maximum Aposteriori Probability (MAP). Solid lines are marginal probability densities for K_2 and T , dashed line corresponds to K_1 . Red lines correspond to parameters combination allowing to predict the ^{10}Be and ^{26}Al concentrations within 1σ of the measured values (K_1 is set at $4 \times 10^{-5} \text{ m}^2/\text{a}$). Red filled circle is a manually set parameters combination. (B) Marine $\delta^{18}\text{O}$ stack from Lisiecki and Raymo [2005] (log time scale). (C) Comparison of hilltop curvature (C_{HT}) and ^{10}Be concentrations. Grey lines are predictions for different time-constant sediment transport coefficients scenarios. Blue and red curves correspond to the predictions associated with sets of parameters from the filled circles on panel A. Dark green curve corresponds to the predictions with a sediment transport coefficient evolution mapped on the $\delta^{18}\text{O}$ curve, ranging from 10^{-5} to $3 \times 10^{-4} \text{ m}^2/\text{a}$.

395 length with a 10^4 length burn-in phase. The multivariate Potential Scale Reduction Factor
 396 is 1.001 suggesting convergence was achieved [Gelman and Rubin, 1992].

397 The inversion results support a low initial K value ($< 8 \times 10^{-5} \text{ m}^2/\text{a}$), followed by a very
 398 marked increase (5×10^{-5} to $5 \times 10^{-4} \text{ m}^2/\text{a}$). A pronounced trade-off exists between the
 399 onset time of the second phase and the value of its sediment transport coefficient, which
 400 makes it difficult to directly confront these results with climatological and morphological
 401 records. Indeed, both an intense and recent phase with a transition as young as 10 ka or
 402 a much older up to 1 Ma event with lower sediment transport coefficient could provide

403 reasonable fits to the data (Fig. 8B). We note that solving for TCN accumulation using an
404 simplified Eulerian approach [Knudsen et al., 2019] with exponential attenuation profile for
405 muonic production and a time-independent scaling [Stone, 2000], instead of the Lagrangian
406 scheme we used in our reference model, does not substantially modify the outcome of the
407 inversion (Fig. 9B).

408 Additional independent constraints can be obtained from the low $^{26}\text{Al}/^{10}\text{Be}$ ratios of the
409 fastest denudation sites. Assuming an initial $K_1 = 4 \times 10^{-5} \text{ m}^2/\text{a}$, for each value of K_2 we
410 computed the best transition time T allowing to explain both ^{10}Be and ^{26}Al concentra-
411 tions within 1σ uncertainty, for each sample independently (Fig. 8A, red lines). For each
412 of these samples (M, U, V), we observed the same tradeoff between K_2 and T as for the
413 C_{HT} - ^{10}Be inversion of the whole dataset. The lines defining the best K_2 - T combinations
414 for these ^{26}Al - ^{10}Be data appears to intersect the region of maximum posterior density for
415 the C_{HT} - ^{10}Be inversion at a transition time $T \sim 100 \text{ ka}$. Finally, a joint inversion of C_{HT} ,
416 ^{10}Be and ^{26}Al data for the whole dataset narrows down the range of probable transition
417 time and is also consistent with a value close to 100 ka (Fig. 9C). As discussed below,
418 this time scale for a postulated shift in surface dynamics is in agreement with reported
419 environmental changes in the area, notably precipitation [e.g. Cruz et al., 2009b].

420 We note that our results could be affected by the processes occurring during the exhumation
421 of the quartz fragments sampled at the surface. Notably, a mixing of these fragments in the
422 regolith layer, rather than the monotonous exhumation toward the surface assumed in our
423 models, would significantly impact their accumulation of cosmogenic nuclides through time
424 [Granger et al., 1996; Makhubela et al., 2019]. As discussed above, we have numerous lines
425 of evidence that those fragments result from the dismantlement of massive quartz veins,
426 which remained mostly cohesive during their exhumation history embedded in the regolith,
427 implying little mixing. The $^{26}\text{Al}/^{10}\text{Be}$ ratios of most of the high-concentration samples are
428 not compatible with a significant mixing of the fragments in the regolith (Fig 7A), with the

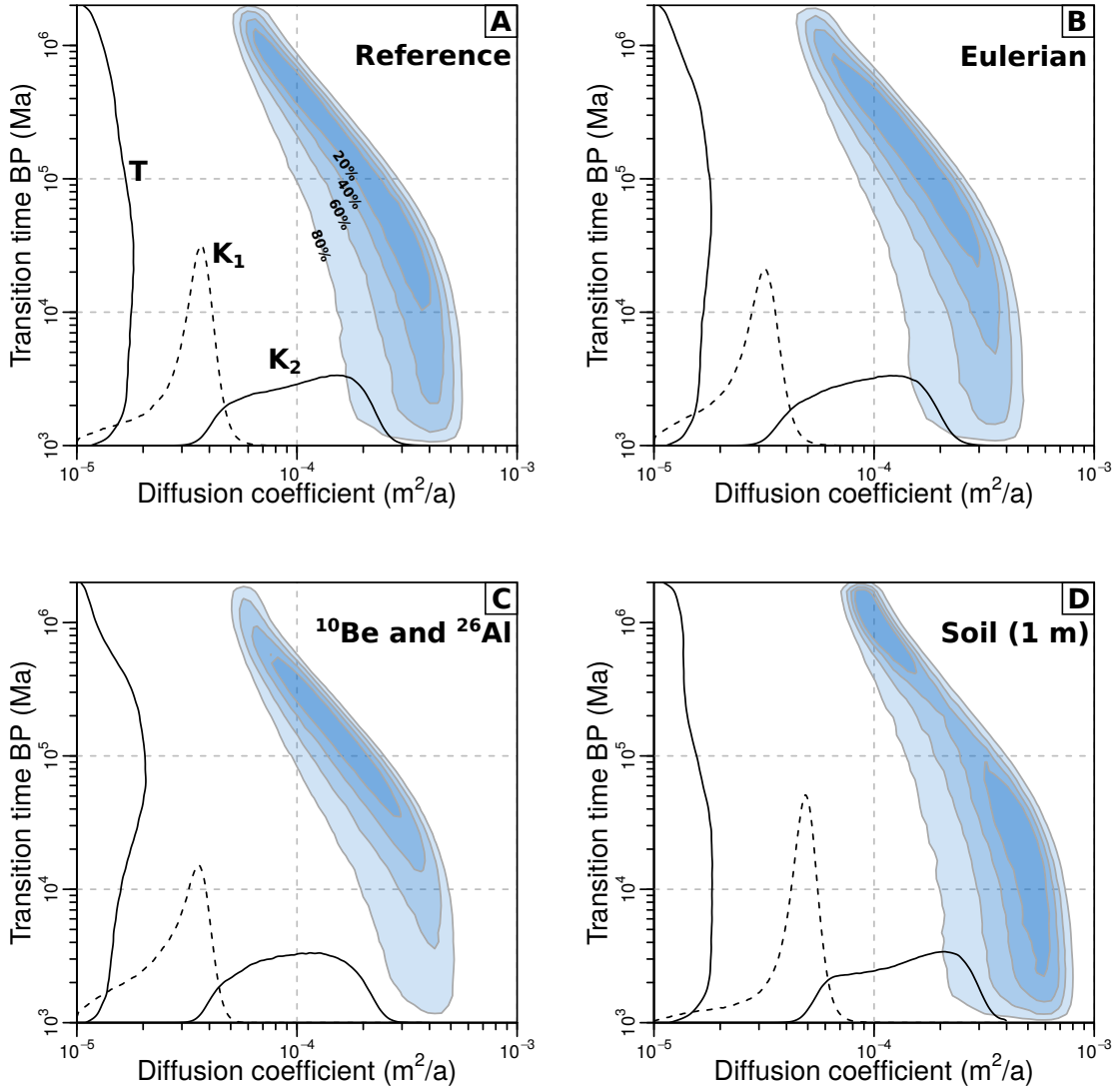


Figure 9: Tests of the influence of various aspects of the modelling approach on the inverted distributions for K_1 , K_2 and T . (A) Reference model (same as Fig. 8). Result of a MCMC inversion based on a 2-stages history set by 3 parameters: the initial (K_1) and final (K_2) sediment transport coefficients and the transition time T between the two. Blue shaded contours are highest posterior density region for T against K_2 . Solid lines are marginal probability density for K_2 and T , dashed line corresponds to K_1 . (B) Same as reference model but forward problem is solved with an Eulerian approach [Knudsen et al., 2019], using the time-independent Stone [2000] scaling and an exponential model for the muonic production at depth, with parameters from Braucher et al. [2011]. This simplified and computationally much faster Eulerian scheme provides essentially the same results as the reference model. (C) Same as reference model but using both ^{10}Be and ^{26}Al concentrations (only ^{10}Be data is used in the reference model). (D) Same as reference model, but the density decreases to 1.7 during the last 1 m of the exhumation history, to test the influence of density change associated with a regolith layer.

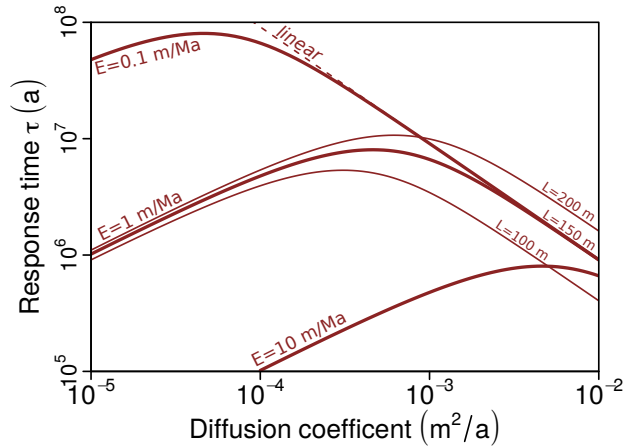


Figure 10: Adjustment time-scales of hillslopes based on linear (dashed lines) and non-linear (solid lines) evolution models [Roering et al., 2001; Hurst et al., 2012], for different values of the erosion rate E and hillslope length L .

429 exception of sample Q. We also note that our reference model is designed with a constant
 430 density during the exhumation history. In order to test the influence of a change in density
 431 when moving through the regolith for the final stage of exhumation [Struck et al., 2018],
 432 we tested the effect of a 1-m thick layer of density 1.7, and we observed that such mod-
 433 ification does not substantially alter the general pattern retrieved from the inversion for
 434 the various parameters (Fig. 9D). It is important to note that our approach relies on the
 435 hypothesis that hillslope morphology does not change substantially over the investigated
 436 time period, so that there is no feedback between denudation and hilltop curvature, which
 437 is considered constant here. Calculated hillslope response times for the range of very low
 438 denudation rates and sediment transport coefficient considered here are at least several
 439 Ma, supporting the hypothesis of a stable landscape over the time-frame of the climatic
 440 perturbations scenarios we investigate (Fig. 10).

441 6.3 Comparison with regional climatic and geomorphic records

442 The two types of observations we made (C_{HT} - ^{10}Be relationship and $^{26}\text{Al}/^{10}\text{Be}$ ratios) sug-
 443 gest a significant increase of denudation occurring over the last few 100s ka. However, it

444 is difficult to pinpoint an actual event from each approach alone. Indeed, onset of rapid
445 denudation as young as a few 10s ka, close to the Last Glacial Maximum, or as old as
446 800 ka, near the Mid-Pleistocene Transition, provide comparable fits to the C_{HT} - ^{10}Be data
447 (Fig. 8). We note that we also used a very simplified 3-parameters definition of the evolu-
448 tion of K , which implies a single step-change and does not allow the possibility of multiple
449 events or of a gradual change. We tested this type of scenario by mapping the evolution of
450 the sediment transport coefficient on the $\delta^{18}\text{O}$ stack of [Lisiecki and Raymo \[2005\]](#), with a
451 prescribed range of variations. Such evolution of K yields a relationship between C_{HT} and
452 ^{10}Be concentrations that does not fit the data as well as the abrupt evolution associated
453 with the 3-parameters scenarios. However, it still reproduces the general trend and in
454 particular the fact that it does not correspond to a steady state situation (Fig. 8C, green
455 line). When considered alone, the $^{26}\text{Al}/^{10}\text{Be}$ ratios of the high-denudation samples also
456 display a similar tradeoff between T and K_2 , but the combination with C_{HT} - ^{10}Be inversion
457 results significantly narrows down the range of likely age for the onset of the increase in
458 denudation rates to 100-300 ka (Figs. 8 and S4).

459 There are lines of evidence supporting important Quaternary fluctuations of precipitation,
460 temperature and vegetation in SE Brazil [[Salgado-Labouriau et al., 1998](#); [Behling, 2002](#);
461 [Ledru et al., 2005](#)], and in particular in the Espinhaço Range [[Chueng et al., 2019](#); [Silva
462 et al., 2020](#)]. For example, precipitation has been shown to be strongly modulated by
463 orbital fluctuations [[Wang et al., 2007](#); [Cruz et al., 2009a](#)], with some speleothem records
464 suggesting a wetter climate starting at 70 ka [[Cruz et al., 2009b](#)], a timing comparable
465 with the transition time inferred from our inversion results. Early and Middle Quater-
466 nary geomorphological markers, such as river terraces, are often poorly preserved in the
467 area, but display a strong climatic control on cycles of erosion and deposition [[Barros and
468 Magalhães Junior, 2020](#)]. The hypothesis that climatic fluctuations is the main driver of
469 the increase in denudation rates is reinforced by the fact that there was a reduction in in-

470 traplate tectonic activity beginning in the Middle Quaternary or earlier in the southeastern
471 highlands of Brazil [Salgado et al., 2016]. This idea of a dominant climatic control is further
472 reinforced by the non-linear $E-C_{HT}$ relationship observed in figure 7, which can be consid-
473 ered as symptomatic of a top-down climatic forcing, where climatically-triggered changes in
474 precipitation or vegetation modulate hillslope sediment transport coefficient. Conversely, a
475 bottom-up perturbation associated with tectonically-driven base level changes would pre-
476 serve the co-linearity of the samples in an $E-C_{HT}$ plot. While we cannot unambiguously
477 associate a particular event to our observations of transience in the landscape of the Serra
478 do Cipó, they probably result from the integration of climatic fluctuations and an increased
479 denudation trend over the Late Pleistocene.

480 **6.4 Implications for the detection of transient evolution in land-** 481 **scapes**

482 Combining the analysis of detailed high resolution hillslope morphometry with TCN data
483 is a promising way to investigate landscape dynamics but has been only used in a limited
484 number of situations [DiBiase et al., 2012; Hurst et al., 2012; Godard et al., 2019, 2020].
485 Such an approach allows to combine the two types of observation into a physical, process-
486 based framework, such as equation 5, in order to test the underlying assumption and
487 evaluate its limitations. Our study illustrates the potential of such an approach to identify
488 transient dynamics in slowly eroding landscapes, and assess its links with climatically-
489 driven top-down forcings. We take advantage of the differences in integration timescales of
490 the two methods: a few 100 ka for TCN concentrations and of the order of 1 Ma for hilltop
491 curvature measurements (Fig. 10), which allows to unravel time variations in the intensity
492 of surface processes. Hilltops of the Serra do Cipó range display several evidences of Late
493 Quaternary acceleration of erosion, as the relationship between ^{10}Be concentrations and

494 hilltop morphology, as well as the $^{26}\text{Al}/^{10}\text{Be}$ ratios, both displaying significant deviation
495 from steady state predictions. There are however limits to the resolving power of such com-
496 bination with respect to the details of denudation history that can be retrieved, which are
497 manifest in the observed trade-offs between parameters (Fig 8A and 9). Using additional
498 TCN, such ^{36}Cl or *in situ* ^{14}C might allow to extract more details about the denudation
499 history. However, *in situ* ^{14}C has not yet been used to investigate such low denudation
500 settings and modeling studies anticipate important limitations to its resolving power in
501 such settings [Skov et al., 2019]. ^{36}Cl would require target minerals such as carbonates
502 or feldspars which are not present in the setting we investigated, but might be feasible in
503 granitic landscapes. While it does not provide a time-series for the evolution of denuda-
504 tion, our study illustrates the possibilities and potential of investigating paleo-denudation
505 of slowly evolving landscapes in addition to the often explored tectonically active mountain
506 ranges.

507 7 Conclusion

508 We studied the denudation of hilltop sites in the Serra do Cipó range, by collecting high
509 resolution morphometric data and measuring ^{10}Be and ^{26}Al concentrations in surface mate-
510 rials. We compared our observations with prediction of simple hillslope diffusion theory for
511 the relationship between morphological attributes and denudation rates derived from these
512 TCN concentrations. We identified substantial deviation from steady state configuration,
513 suggesting an important change in surface denudation over recent time periods, which re-
514 sults in the observed transient state. The originality of our approach is to conduct a joint
515 inversion of both isotopic and morphometric data to derive the temporal evolution of the
516 hillslope sediment transport coefficient. Our inversions suggest an important increase in
517 the sediment transport coefficient and denudation rate over 100 ka timescale, which most

518 likely results from a modulation of soil transport efficiency of climatic origin. However, a
519 trade-off between the timing of the acceleration and denudation intensity limits our ability
520 to precisely pin point a specific climatic event. Our study illustrates the strong poten-
521 tial of landscape analysis that link geochronological and topographic data into a single
522 physically-based framework, as for example hillslope diffusion theory. In our case, it allows
523 to identify transient dynamics at the scale of hillslope, and the persistence of instabilities,
524 which is key for longer-wavelength landscape-scale analysis of the influence of climatic and
525 tectonic forcings.

526 **Acknowledgments**

527 This work was supported by CAPES-COFECUB (Research Project 869/15) and an IUF
528 fellowship to VG. The ^{10}Be and ^{26}Al measurements were performed at the ASTER AMS
529 national facility (CEREGE, Aix en Provence) which is supported by the INSU/CNRS,
530 the ANR through the "Projets thématiques d'excellence" program for the "Equipements
531 d'excellence" ASTER-CEREGE action and IRD. The Pléiades images used in this study
532 were obtained through the DINAMIS framework and GEOSUD EQUIPEX. We thank
533 Rodolphe Cattin for insightful discussions. Constructive comments by Simon Mudd, an
534 anonymous reviewer and the associate editor greatly helped to improve this manuscript.
535 This article is dedicated to the memory of our friend and colleague Didier L. Bourlès who
536 sadly passed away during its preparation.

537 **References**

- 538 Anderson, R. S. (2002). Modeling the tor-dotted crests, bedrock edges, and parabolic
539 profiles of high alpine surfaces of the Wind River Range, Wyoming. *Geomorphology*,
540 46(1-2):35–58.
- 541 Ansberque, C., Bellier, O., Godard, V., Lasserre, C., Wang, M., Braucher, R., Talon, B.,

- 542 de Sigoyer, J., Xu, X., and Bourlès, D. L. (2016). The Longriqu fault zone, eastern
543 Tibetan Plateau: Segmentation and Holocene behavior. *Tectonics*, 35(3):565–585.
- 544 Arnold, M., Merchel, S., Bourlès, D. L., Braucher, R., Benedetti, L., Finkel, R. C.,
545 Aumaître, G., Gottdang, A., and Klein, M. (2010). The French accelerator mass spec-
546 trometry facility ASTER: Improved performance and developments. *Nuclear Instru-
547 ments and Methods in Physics Research, Section B: Beam Interactions with Materials
548 and Atoms*, 268(11-12):1954–1959. ISBN: 0168-583X.
- 549 Balco, G. (2017). Production rate calculations for cosmic-ray-muon-produced ^{10}Be and
550 ^{26}Al benchmarked against geological calibration data. *Quaternary Geochronology*,
551 39:150–173. Publisher: Elsevier B.V.
- 552 Balco, G., Stone, J. O., Lifton, N. a., and Dunai, T. J. (2008). A complete and easily
553 accessible means of calculating surface exposure ages or erosion rates from ^{10}Be and
554 ^{26}Al measurements. *Quaternary Geochronology*, 3(3):174–195. ISBN: 1871-1014.
- 555 Barreto, H. N., Varajão, C. A., Braucher, R., Bourlès, D. L., Salgado, A. A., and Varajão,
556 A. F. (2013). Denudation rates of the Southern Espinhaço Range, Minas Gerais, Brazil,
557 determined by in situ-produced cosmogenic beryllium-10. *Geomorphology*, 191:1–13.
- 558 Barros, L. F. d. P. and Magalhães Junior, A. P. (2020). Late quaternary landscape evolution
559 in the Atlantic Plateau (Brazilian highlands): Tectonic and climatic implications of
560 fluvial archives. *Earth-Science Reviews*, 207(May):103228. Publisher: Elsevier.
- 561 Behling, H. (2002). South and southeast Brazilian grasslands during Late Quaternary
562 times: A synthesis. *Palaeogeography, Palaeoclimatology, Palaeoecology*, 177(1-2):19–27.
- 563 Bernard, M., Decluseau, D., Gabet, L., and Nonin, P. (2012). 3D capabilities of PLEIADES
564 satellite. *ISPRS - International Archives of the Photogrammetry, Remote Sensing and
565 Spatial Information Sciences*, XXXIX-B3:553–557.
- 566 Borchers, B., Marrero, S., Balco, G., Caffee, M., Goehring, B., Lifton, N., Nishiizumi,
567 K., Phillips, F., Schaefer, J., and Stone, J. (2016). Geological calibration of spallation
568 production rates in the CRONUS-Earth project. *Quaternary Geochronology*, 31:188–198.
569 Publisher: Elsevier B.V ISBN: 4025594390.
- 570 Braucher, R., Guillou, V., Bourlès, D. L., Arnold, M., Aumaître, G., Keddadouche, K.,
571 and Nottoli, E. (2015). Preparation of ASTER in-house $^{10}\text{Be}/^{9}\text{Be}$ standard solutions.
572 *Nuclear Instruments and Methods in Physics Research Section B: Beam Interactions
573 with Materials and Atoms*, 361:335–340.
- 574 Braucher, R., Merchel, S., Borgomano, J., and Bourlès, D. (2011). Production of cosmo-
575 genic radionuclides at great depth: A multi element approach. *Earth and Planetary
576 Science Letters*, 309(1-2):1–9.

- 577 Brown, E. T., Edmond, J. M., Raisbeck, G. M., Yiou, F., Kurz, M. D., and Brook,
578 E. J. (1991). Examination of surface exposure ages of Antarctic moraines using in situ
579 produced ^{10}Be and ^{26}Al . *Geochimica et Cosmochimica Acta*, 55(8):2269–2283. ISBN:
580 0016-7037.
- 581 Broxton, M. and Edwards, L. (2008). The Ames Stereo Pipeline: Automated 3D Surface
582 Reconstruction from Orbital Imagery. In *Lunar and Planetary Science Conference*,
583 volume 39, page 2419, League City, Texas. Series Title: Lunar and Planetary Science
584 Conference.
- 585 Champagnac, J.-D., Molnar, P., Sue, C., and Herman, F. (2012). Tectonics, climate, and
586 mountain topography. *Journal of Geophysical Research*, 117(B2):B02403.
- 587 Charreau, J., Blard, P.-H., Puchol, N., Avouac, J.-P., Lallier-Vergès, E., Bourlès, D.,
588 Braucher, R., Gallaud, A., Finkel, R., Jolivet, M., Chen, Y., and Roy, P. (2011). Paleo-
589 erosion rates in Central Asia since 9Ma: A transient increase at the onset of Quaternary
590 glaciations? *Earth and Planetary Science Letters*, 304(1-2):85–92.
- 591 Chueng, K. F., Gomes Coe, H. H., Ribeiro Rocha Augustin, C. H., Macario, K. D.,
592 Fricks Ricardo, S. D., and Carvalho Vasconcelos, A. M. (2019). Landscape paleody-
593 namics in siliciclastic domains with the use of phytoliths, sponge spicules and carbon
594 isotopes: The case of southern Espinhaço Mountain Range, Minas Gerais, Brazil. *Jour-
595 nal of South American Earth Sciences*, 95(April):102232. Publisher: Elsevier.
- 596 Cruz, F. W., Vuille, M., Burns, S. J., Wang, X., Cheng, H., Werner, M., Lawrence Edwards,
597 R., Karmann, I., Auler, A. S., and Nguyen, H. (2009a). Orbitally driven east-west an-
598 tiphasing of South American precipitation. *Nature Geoscience*, 2(3):210–214. Publisher:
599 Nature Publishing Group.
- 600 Cruz, F. W., Wang, X., Auler, A., Vuille, M., Burns, S. J., Edwards, L. R., Karmann, I.,
601 and Cheng, H. (2009b). Orbital and Millennial-Scale Precipitation Changes in Brazil
602 from Speleothem Records. In Vimeux, F., Sylvestre, F., and Khodri, M., editors, *Past
603 Climate Variability in South America and Surrounding Regions*, volume 14, pages 29–
604 60. Springer Netherlands, Dordrecht. Series Title: Developments in Paleoenvironmental
605 Research.
- 606 DiBiase, R. A., Heimsath, A. M., and Whipple, K. X. (2012). Hillslope response to tectonic
607 forcing in threshold landscapes. *Earth Surface Processes and Landforms*, 37(8):855–865.
- 608 DiBiase, R. A., Whipple, K. X., Heimsath, A. M., and Ouimet, W. B. (2010). Landscape
609 form and millennial erosion rates in the San Gabriel Mountains, CA. *Earth and Planetary
610 Science Letters*, 289(1-2):134–144.
- 611 Dietrich, W. E., Bellugi, D. G., Sklar, L. S., Stock, J. D., Heimsath, A. M., and Roering,
612 J. J. (2003). Geomorphic transport laws for predicting landscape form and dynamics.
613 In Wilcock, P. R. and Iverson, R. M., editors, *Prediction in Geomorphology*, volume

- 614 135, pages 103–132. American Geophysical Union, Washington, D. C. Series Title:
615 Geophysical Monograph Series ISSN: 0065-8448.
- 616 Foster, M. A., Anderson, R. S., Wyshnytzky, C. E., Ouimet, W. B., and Dethier, D. P.
617 (2015). Hillslope lowering rates and mobile-regolith residence times from in situ and
618 meteoric ^{10}Be analysis, Boulder Creek Critical Zone Observatory, Colorado. *Geological*
619 *Society of America Bulletin*, 127(5):862–878.
- 620 Fox, M., Bodin, T., and Shuster, D. L. (2015). Abrupt changes in the rate of Andean
621 Plateau uplift from reversible jump Markov Chain Monte Carlo inversion of river profiles.
622 *Geomorphology*, 238:1–14. Publisher: Elsevier B.V.
- 623 Gabet, E. J., Burbank, D. W., Pratt-Sitaula, B., Putkonen, J., and Bookhagen, B. (2008).
624 Modern erosion rates in the High Himalayas of Nepal. *Earth and Planetary Science*
625 *Letters*, 267(3-4):482–494. ISBN: 0012-821X.
- 626 Gabet, E. J., Mudd, S. M., Wood, R. W., Grieve, S. W. D., Binnie, S. A., and Dunai,
627 T. J. (2021). Hilltop Curvature Increases with the Square Root of Erosion Rate.
628 *Journal of Geophysical Research: Earth Surface*, n/a(n/a):e2020JF005858. eprint:
629 <https://onlinelibrary.wiley.com/doi/pdf/10.1029/2020JF005858>.
- 630 Gaillardet, J., Dupré, B., Louvat, P., and Allègre, C. (1999). Global silicate weathering and
631 CO_2 consumption rates deduced from the chemistry of large rivers. *Chemical Geology*,
632 159(1-4):3–30.
- 633 Gelman, A. and Rubin, D. B. (1992). Inference from Iterative Simulation Using Multiple
634 Sequences. *Statistical Science*, 7(4):457–472. arXiv: 1011.1669 ISBN: 0883-4237.
- 635 Godard, V., Dosseto, A., Fleury, J., Bellier, O., Siame, L., and ASTER, T. (2019). Tran-
636 sient landscape dynamics across the Southeastern Australian Escarpment. *Earth and*
637 *Planetary Science Letters*, 506:397–406. Publisher: Elsevier B.V.
- 638 Godard, V., Hippolyte, J.-C., Cushing, E., Espurt, N., Fleury, J., Bellier, O., and Ollivier,
639 V. (2020). Hillslope denudation and morphologic response to a rock uplift gradient.
640 *Earth Surface Dynamics*, 8(2):221–243.
- 641 Godard, V., Ollivier, V., Bellier, O., Miramont, C., Shabanian, E., Fleury, J., Benedetti, L.,
642 and Guillou, V. (2016). Weathering-limited hillslope evolution in carbonate landscapes.
643 *Earth and Planetary Science Letters*, 446:10–20. Publisher: Elsevier B.V.
- 644 Granger, D. E., Kirchner, J. W., and Finkel, R. (1996). Spatially averaged long-term
645 erosion rates measured from in situ-produced cosmogenic nuclides in alluvial sediment.
646 *The Journal of Geology*, 104(3):249–257.
- 647 Granger, D. E. and Muzikar, P. F. (2001). Dating sediment burial with in situ-produced
648 cosmogenic nuclides: theory, techniques, and limitations. *Earth and Planetary Science*
649 *Letters*, 188(1-2):269–281. ISBN: 0012-821X.

- 650 Grieve, S. W., Mudd, S. M., and Hurst, M. D. (2016a). How long is a hillslope? *Earth*
651 *Surface Processes and Landforms*, 41(8):1039–1054.
- 652 Grieve, S. W. D., Mudd, S. M., Hurst, M. D., and Milodowski, D. T. (2016b). A nondi-
653 mensional framework for exploring the relief structure of landscapes. *Earth Surface*
654 *Dynamics*, 4(2):309–325.
- 655 Hales, T. C. and Roering, J. J. (2005). Climate-controlled variations in scree production,
656 Southern Alps, New Zealand. *Geology*, 33(9):701–704.
- 657 Herman, F. and Champagnac, J.-D. (2016). Plio-Pleistocene increase of erosion rates in
658 mountain belts in response to climate change. *Terra Nova*, 28(1):2–10.
- 659 Hippe, K. (2017). Constraining processes of landscape change with combined in situ cosmo-
660 genic ^{14}C - ^{10}Be analysis. *Quaternary Science Reviews*, 173:1–19. Publisher: Elsevier
661 Ltd.
- 662 Hippe, K., Jansen, J. D., Skov, D. S., Lupker, M., Ivy-Ochs, S., Kober, F., Zeilinger, G.,
663 Capriles, J. M., Christl, M., Maden, C., Vockenhuber, C., and Egholm, D. L. (2021).
664 Cosmogenic in situ ^{14}C - ^{10}Be reveals abrupt Late Holocene soil loss in the Andean Alti-
665 toplano. *Nature Communications*, 12(1):2546. Number: 1 Publisher: Nature Publishing
666 Group.
- 667 Hurst, M. D., Mudd, S. M., Attal, M., and Hilley, G. (2013). Hillslopes record the growth
668 and decay of landscapes. *Science*, 341(6148):868–871.
- 669 Hurst, M. D., Mudd, S. M., Walcott, R., Attal, M., and Yoo, K. (2012). Using hilltop
670 curvature to derive the spatial distribution of erosion rates. *Journal of Geophysical*
671 *Research*, 117(F2):F02017.
- 672 Knudsen, M. F. and Egholm, D. L. (2018). Constraining Quaternary ice covers and erosion
673 rates using cosmogenic $^{26}\text{Al}/^{10}\text{Be}$ nuclide concentrations. *Quaternary Science Reviews*,
674 181:65–75. Publisher: Elsevier Ltd.
- 675 Knudsen, M. F., Egholm, D. L., and Jansen, J. D. (2019). Time-integrating cosmogenic nu-
676 chloride inventories under the influence of variable erosion, exposure, and sediment mixing.
677 *Quaternary Geochronology*, 51(December 2018):110–119. Publisher: Elsevier.
- 678 Laloy, E., Beerten, K., Vanacker, V., Christl, M., Rogiers, B., and Wouters, L. (2017).
679 Bayesian inversion of a CRN depth profile to infer Quaternary erosion of the northwestern
680 Campine Plateau (NE Belgium). *Earth Surface Dynamics*, 5(3):331–345.
- 681 Lashermes, B., Fofoula-Georgiou, E., and Dietrich, W. E. (2007). Channel network ex-
682 traction from high resolution topography using wavelets. *Geophysical Research Letters*,
683 34(23):L23S04. ISBN: 0094-8276.

- 684 Ledru, M. P., Rousseau, D. D., Cruz, F. W., Riccomini, C., Karmann, I., and Martin, L.
685 (2005). Paleoclimate changes during the last 100,000 yr from a record in the Brazil-
686 ian Atlantic rainforest region and interhemispheric comparison. *Quaternary Research*,
687 64(3):444–450.
- 688 Lenard, S. J., Lavé, J., France-Lanord, C., Aumaître, G., Bourlès, D. L., and Keddadouche,
689 K. (2020). Steady erosion rates in the Himalayas through late Cenozoic climatic changes.
690 *Nature Geoscience*, 13(6):448–452. Publisher: Springer US.
- 691 Lifton, N., Sato, T., and Dunai, T. J. (2014). Scaling in situ cosmogenic nuclide produc-
692 tion rates using analytical approximations to atmospheric cosmic-ray fluxes. *Earth and*
693 *Planetary Science Letters*, 386:149–160. Publisher: Elsevier B.V.
- 694 Lisiecki, L. E. and Raymo, M. E. (2005). A Pliocene-Pleistocene stack of 57 globally
695 distributed benthic $\delta^{18}\text{O}$ records. *Paleoceanography*, 20(1):PA1003. Publisher: American
696 Geophysical Union.
- 697 Magalhães Junior, A. P., de Paula Barros, L. F., and Felipe, M. F. (2015). Southern Serra
698 do Espinhaço: The Impressive Plateau of Quartzite Ridges. In Vieira, B. C., Salgado, A.
699 A. R., and Santos, L. J. C., editors, *Landscapes and landforms of Brazil*, pages 359–370.
700 Springer. ISSN: 22132104.
- 701 Makhubela, T., Kramers, J., Scherler, D., Wittmann, H., Dirks, P., and Winkler, S. (2019).
702 Effects of long soil surface residence times on apparent cosmogenic nuclide denudation
703 rates and burial ages in the Cradle of Humankind, South Africa. *Earth Surface Processes*
704 *and Landforms*, 44(15):2968–2981.
- 705 Merchel, S., Arnold, M., Aumaître, G., Benedetti, L., Bourlès, D., Braucher, R., Alfimov,
706 V., Freeman, S., Steier, P., and Wallner, A. (2008). Towards more precise ^{10}Be and
707 ^{36}Cl data from measurements at the 10-14 level: Influence of sample preparation. *Nu-*
708 *clear Instruments and Methods in Physics Research Section B: Beam Interactions with*
709 *Materials and Atoms*, 266(22):4921–4926.
- 710 Merchel, S. and Bremser, W. (2004). First international ^{26}Al interlaboratory compari-
711 son - Part I. *Nuclear Instruments and Methods in Physics Research Section B: Beam*
712 *Interactions with Materials and Atoms*, 223-224:393–400. Publisher: North-Holland.
- 713 Metropolis, N., Rosenbluth, A. W., Rosenbluth, M. N., Teller, A. H., and Teller, E. (1953).
714 Equation of State Calculations by Fast Computing Machines. *The Journal of Chemical*
715 *Physics*, 21(6):1087–1092.
- 716 Moratto, Z., Broxton, M., Beyer, R., Lundy, M., and Husmann, K. (2010). Ames Stereo
717 Pipeline, NASA’s Open Source Automated Stereogrammetry Software. In *Lunar and*
718 *Planetary Science Conference*, volume 41, page 2364, The Woodlands, Texas. Series
719 Title: Lunar and Planetary Science Conference.

- 720 Mudd, S. M. (2016). Detection of transience in eroding landscapes. *Earth Surface Processes*
721 *and Landforms*, 42(1):24–41. ISBN: 0197-9337.
- 722 Nefian, A. V., Husmann, K., Broxton, M., To, V., Lundy, M., and Hancher, M. D. (2009).
723 A bayesian formulation for sub-pixel refinement in stereo orbital imagery. In *2009 16th*
724 *IEEE International Conference on Image Processing (ICIP)*, pages 2361–2364, Cairo,
725 Egypt. IEEE.
- 726 Norton, K. P. and Schlunegger, F. (2017). Lack of a weathering signal with increased
727 Cenozoic erosion? *Terra Nova*, 29(5):265–272.
- 728 Ouimet, W. B., Whipple, K. X., and Granger, D. E. (2009). Beyond threshold hillslopes:
729 Channel adjustment to base-level fall in tectonically active mountain ranges. *Geology*,
730 37(7):579–582. Publisher: Geological Society of America.
- 731 Peifer, D., Persano, C., Hurst, M. D., Bishop, P., and Fabel, D. (2020). Growing topography
732 due to contrasting rock types in a tectonically dead landscape. *Earth Surface Dynamics*
733 *Discussions*, 2020:1–29.
- 734 Roberts, G. G. and White, N. (2010). Estimating uplift rate histories from river profiles
735 using African examples. *Journal of Geophysical Research*, 115(B2):B02406.
- 736 Roering, J. J., Almond, P., Tonkin, P., and McKean, J. (2004). Constraining climatic
737 controls on hillslope dynamics using a coupled model for the transport of soil and trac-
738 ers: Application to loess-mantled hillslopes, South Island, New Zealand. *Journal of*
739 *Geophysical Research*, 109(F1):F01010. ISBN: 0148-0227.
- 740 Roering, J. J., Kirchner, J. W., and Dietrich, W. E. (1999). Evidence for nonlinear,
741 diffusive sediment transport on hillslopes and implications for landscape morphology.
742 *Water Resources Research*, 35(3):853–870. Publisher: American Geophysical Union.
- 743 Roering, J. J., Kirchner, J. W., and Dietrich, W. E. (2001). Hillslope evolution by nonlin-
744 ear, slope-dependent transport: Steady state morphology and equilibrium adjustment
745 timescales. *Journal of Geophysical Research*, 106(B8):16499–16513. ISBN: 0148-0227.
- 746 Roering, J. J., Marshall, J., Booth, A. M., Mort, M., and Jin, Q. (2010). Evidence for
747 biotic controls on topography and soil production. *Earth and Planetary Science Letters*,
748 298(1-2):183–190. Publisher: Elsevier B.V. ISBN: 0012-821X.
- 749 Roering, J. J., Perron, J. T., and Kirchner, J. W. (2007). Functional relationships between
750 denudation and hillslope form and relief. *Earth and Planetary Science Letters*, 264(1-
751 2):245–258.
- 752 Salgado, A. A. R., Rezende, E. d. A., Boursès, D., Braucher, R., da Silva, J. R., and Garcia,
753 R. A. (2016). Relief evolution of the Continental Rift of Southeast Brazil revealed by in
754 situ-produced ^{10}Be concentrations in river-borne sediments. *Journal of South American*
755 *Earth Sciences*, 67:89–99.

- 756 Salgado, A. A. R., Santos, L. J. C., and Paisani, J. C. (2019). *The physical geography of*
757 *Brazil*. Springer. Publication Title: Springer.
- 758 Salgado-Labouriau, M. L., Barberi, M., Ferraz-Vicentini, K. R., and Parizzi, M. G. (1998).
759 A dry climatic event during the late Quaternary of tropical Brazil. *Review of Palaeob-*
760 *otany and Palynology*, 99(2):115–129.
- 761 Silva, A. C., Horák-Terra, I., Barral, U. M., Costa, C. R., Gonçalves, S. T., Pinto, T.,
762 Christófaró Silva, B. P., Cunha Fernandes, J. S., Mendonça Filho, C. V., and Vidal-
763 Torrado, P. (2020). Altitude, vegetation, paleoclimate, and radiocarbon age of the basal
764 layer of peatlands of the Serra do Espinhaço Meridional, Brazil. *Journal of South Amer-*
765 *ican Earth Sciences*, 103(June):102728.
- 766 Skov, D. S., Egholm, D. L., Jansen, J. D., Sandiford, M., and Knudsen, M. F. (2019).
767 Detecting landscape transience with in situ cosmogenic ^{14}C and ^{10}Be . *Quaternary*
768 *Geochronology*, 54(June):101008.
- 769 Stone, J. O. (2000). Air pressure and cosmogenic isotope production. *Journal of Geophys-*
770 *ical Research: Solid Earth*, 105(B10):23753–23759. Publisher: American Geophysical
771 Union.
- 772 Struck, M., Jansen, J. D., Fujioka, T., Codilean, A. T., Fink, D., Egholm, D. L., Fülöp,
773 R.-H., Wilcken, K. M., and Kotevski, S. (2018). Soil production and transport on
774 postorogenic desert hillslopes quantified with ^{10}Be and ^{26}Al . *GSA Bulletin*, 130(5-
775 6):1017–1040.
- 776 von Blanckenburg, F. (2005). The control mechanisms of erosion and weathering at basin
777 scale from cosmogenic nuclides in river sediment. *Earth and Planetary Science Letters*,
778 237(3-4):462–479.
- 779 Wang, X., Auler, A. S., Edwards, R. L., Cheng, H., Ito, E., Wang, Y., Kong, X., and
780 Solheid, M. (2007). Millennial-scale precipitation changes in southern Brazil over the
781 past 90,000 years. *Geophysical Research Letters*, 34(23):L23701. Publisher: American
782 Geophysical Union.
- 783 West, N., Kirby, E., Bierman, P., and Clarke, B. A. (2014). Aspect-dependent variations
784 in regolith creep revealed by meteoric ^{10}Be . *Geology*, 42(6):507–510.
- 785 Willenbring, J. K. and Jerolmack, D. J. (2016). The null hypothesis: globally steady rates
786 of erosion, weathering fluxes and shelf sediment accumulation during Late Cenozoic
787 mountain uplift and glaciation. *Terra Nova*, 28(1):11–18.

Table 1: Cosmogenic nuclides data : ^{10}Be results

Mass ^e (g)	Be carrier ^b (g)	$^{10}\text{Be}/^9\text{Be}^{c,d,e,f}$ ($\times 10^{-12}$)	$[^{10}\text{Be}]^d$ ($\times 10^6$ at/g)	^{10}Be denudation rate ^{d,g,h} (m/Ma)	τ^i (Ma)	
M	16.22	0.1521	0.624 \pm 0.013	1.176 \pm 0.024	3.69 \pm 0.33 (3.46)	0.2
N	16.84	0.1531	1.23 \pm 0.02	2.254 \pm 0.037	1.84 \pm 0.17 (1.67)	0.3
O	9.8	0.153	0.573 \pm 0.014	1.798 \pm 0.045	2.37 \pm 0.24 (2.19)	0.3
P	20.87	0.1529	2.999 \pm 0.048	4.437 \pm 0.071	0.83 \pm 0.09 (0.68)	0.7
Q	21.85	0.1519	4.898 \pm 0.073	6.879 \pm 0.103	0.5 \pm 0.06 (0.33)	1.2
R	21.65	0.1527	5.048 \pm 0.072	7.192 \pm 0.103	0.46 \pm 0.06 (0.29)	1.3
S	21.17	0.1543	3.966 \pm 0.06	5.838 \pm 0.089	0.61 \pm 0.07 (0.45)	1.0
T	17.82	0.1533	5.205 \pm 0.076	9.046 \pm 0.132	0.35 \pm 0.05 (0.18)	1.7
U	20.11	0.1475	0.516 \pm 0.011	0.759 \pm 0.017	6 \pm 0.54 (5.7)	0.1
V	19.77	0.1525	1.139 \pm 0.02	1.77 \pm 0.031	2.32 \pm 0.21 (2.14)	0.3
W	20.02	0.1536	2.902 \pm 0.053	4.495 \pm 0.082	0.82 \pm 0.09 (0.67)	0.7

^a Dissolved pure quartz mass.

^b Be in-house carrier mass, ~ 150 μl at 3.025×10^{-3} g/g [Merchel et al., 2008].

^c $^{10}\text{Be}/^9\text{Be}$ ratios were calibrated against the STD-11 standard by using an assigned value of $1.191 \pm 0.013 \times 10^{-11}$ [Braucher et al., 2015].

^d Uncertainties are reported at the 1σ level.

^e Uncertainties on isotopic ratios are calculated according to the standard error propagation method using the quadratic sum of the relative errors and include a conservative 0.5% external machine uncertainty [Arnold et al., 2010], the uncertainty on the certified standard ratio, a 1σ uncertainty associated to the mean of the standard ratio measurements during the measurement cycles, a 1σ statistical error on counted events and the uncertainty associated with the chemical and analytical blank corrections.

^f One process blank was treated and measured with our samples, yielding a $^{10}\text{Be}/^9\text{Be}$ ratio of $3.53 \pm 0.34 \times 10^{-15}$. It corresponds to an upper 1σ bound of 120×10^3 ^{10}Be atoms for the background level in this blank, which is at least 120 times lower than the number of ^{10}Be atoms in the dissolved sample masses (600 times lower in average over our dataset). ^g Denudation rates were calculated with the online calculator described in Balco et al. [2008] and the nuclide specific LSD scaling scheme [Lifton et al., 2014], using the CRONUS-Earth calibration dataset [Borchers et al., 2016] for the calculation of spallation production rates and muon production rates according to Balco [2017]. We use 160 g/cm² for the effective neutron attenuation length in rock, and a density of 2.65 g/cm³. No shielding correction was considered for the hilltop sites we sampled.

^h Numbers in parenthesis are the denudation rates computed with Lal/Stone time-independent scaling.

ⁱ Integration time scales for ^{10}Be denudation rates [von Blanckenburg, 2005].

Table 2: Cosmogenic nuclides data : ^{26}Al results and comparison with ^{10}Be results from table 1

Sample	[Al] natural ^a (ppm)	Al carrier ^b (g)	$^{26}\text{Al}/^{27}\text{Al}$ ^{c,d,e} ($\times 10^{-12}$)	^{26}Al ^d ($\times 10^6$ at/g)	^{26}Al denudation rate ^f (mm/ka)	τ ^g (Ma)	$^{10}\text{Be}/^{26}\text{Al}$
M	17.8	1.2448	3.749 ± 0.12	7.27 ± 0.236	3.76 ± 0.54	0.2	6.18 ± 0.24
N	16.1	1.2227	7.834 ± 0.199	14.327 ± 0.369	1.67 ± 0.26	0.4	6.36 ± 0.19
O	114.3	0.6983	3.534 ± 0.105	11.589 ± 0.352	2.2 ± 0.34	0.3	6.44 ± 0.25
P	17.3	1.2211	16.83 ± 0.282	24.976 ± 0.43	0.79 ± 0.15	0.8	5.63 ± 0.13
Q	23.2	1.2278	20.568 ± 0.316	30.037 ± 0.475	0.62 ± 0.13	1.0	4.37 ± 0.1
R	60.4	1.0101	31.101 ± 0.484	45.586 ± 0.727	0.32 ± 0.1	1.9	6.34 ± 0.14
S	20.9	1.2229	21.864 ± 0.346	32.577 ± 0.53	0.56 ± 0.12	1.1	5.58 ± 0.12
T	20.7	1.2355	24.249 ± 0.391	43.197 ± 0.716	0.37 ± 0.1	1.6	4.78 ± 0.11
U	17.9	1.1851	3.256 ± 0.098	4.867 ± 0.149	6.05 ± 0.81	0.1	6.41 ± 0.24
V	16.9	1.0800	7.835 ± 0.208	10.91 ± 0.294	2.27 ± 0.34	0.3	6.16 ± 0.2
W	22.0	1.1442	17.57 ± 0.303	26.155 ± 0.462	0.74 ± 0.14	0.8	5.82 ± 0.15

^a Naturally occurring Al measured by ICP-OES. Note the high concentration for sample O, which is the only one from the quartzite bedrock instead of the quartz veins.

^b Al Carrier mass, 993 ± 4 ppm concentration.

^c The measured $^{26}\text{Al}/^{27}\text{Al}$ ratios were normalized to the in-house standard SM-Al-11 whose ratio of $7.401 \pm 0.064 \times 10^{-12}$ [Arnold et al., 2010] has been cross-calibrated against primary standards from a round-robin exercise [Merchel and Bremser, 2004].

^d Uncertainties are reported at the 1σ level.

^e A process blank yielded a ratio of $2.01 \pm 0.45 \times 10^{-14}$. It corresponds to an upper 1σ bound of 730×10^3 ^{26}Al atoms for the background level in this blank, which is at least 130 times lower than the number of ^{26}Al atoms in the dissolved sample masses (610 times lower in average over our dataset)

^f Procedures for the calculation of denudation rates are identical to the ones described in table 1.

^g Integration time scales for ^{26}Al denudation rates [von Blanckenburg, 2005].

Table 3: Site locations and hilltop curvature measurements

Site	Latitude ($^{\circ}$)	Longitude ($^{\circ}$)	Altitude (m)	Hilltop curvature (m^{-1})
M	-19.2637	-43.5558	1313	0.028 ± 0.010
N	-19.2614	-43.5508	1354	0.020 ± 0.008
O	-19.2612	-43.5508	1353	0.039 ± 0.010
P	-19.2361	-43.5058	1355	0.006 ± 0.002
Q	-19.2301	-43.5051	1365	0.005 ± 0.001
R	-19.2119	-43.5027	1335	0.008 ± 0.001
S	-19.1594	-43.5156	1380	0.008 ± 0.003
T	-19.1582	-43.5174	1379	0.007 ± 0.003
U	-19.2206	-43.4989	1337	0.038 ± 0.011
V	-19.2218	-43.4968	1301	0.024 ± 0.007
W	-19.2337	-43.5050	1357	0.014 ± 0.003